

# Tuning parameters of a sea ice model using machine learning

Anton Korosov<sup>1</sup>, Yue Ying<sup>1</sup>, and Einar Ólason<sup>1</sup>

<sup>1</sup>Nansen Environmental and Remote Sensing Centre, Jahnebakken 3, 50007, Bergen, Norway

**Correspondence:** Anton Korosov (anton.korosov@nersc.no)

**Abstract.** We developed a new method for tuning sea ice rheology parameters, which consists of two components: a new metric for characterising sea ice deformation patterns and an ML-based approach for tuning rheology parameters. We applied the new method to tune the brittle Bingham-Maxwell rheology (BBM) parametrisation, which was implemented and used in the next-generation sea-ice model (neXtSIM). As a reference dataset, we used sea ice drift and deformation observations from 5 the Radarsat Geophysical Processing System (RGPS).

The metric characterises a field of sea ice deformation with a vector of values. It includes well-established descriptors such as the mean and standard deviation of deformation, the structure-function of the spatial scaling analysis, and the density and intersection of linear kinematic features (LKF). We added more descriptors to the metric that characterise the pattern of ice deformation, including image anisotropy and Haralick texture features. The developed metric can describe ice deformation 10 from any model or satellite platform.

In the parameter tuning method, we first run an ensemble of neXtSIM members with perturbed rheology parameters and then train a machine-learning model using the simulated data. We provide the descriptors of ice deformation as input to the ML model and rheology parameters as targets. We apply the trained ML model to the descriptors computed from RGPS observations. The developed ML-based method is generic and can be used to tune the parameters of any model.

15 We ran experiments with tens of members and found optimal values for four neXtSIM BBM parameters: scaling parameter for compressive strength ( $P_0 \approx 5.1$  kPa), cohesion at the reference scale ( $c_{\text{ref}} \approx 1.2$  MPa), internal friction angle tangent ( $\mu \approx 0.7$ ), ice-atmosphere drag coefficient ( $C_A \approx 0.00228$ ). A NeXtSIM run with the optimal parametrisation produces maps of sea ice deformation visually indistinguishable from the RGPS observations. These parameters exhibit weak interannual drift related to changes in sea ice thickness and corresponding changes in ice deformation patterns.

## 20 1 Introduction

Sea-ice dynamics in highly compact ice result from the interaction between surface stress on the ice supplied by wind and ocean currents and the emerging internal stress in the ice. In sea-ice models, the internal stress is calculated by a set of equations commonly referred to as rheology. Virtually all large-scale sea-ice models used for sea-ice forecasting and climate modelling use the so-called viscous-plastic (VP) rheology of Hibler (1979), or more numerically efficient derivatives thereof.

25 Additionally, the elastic-plastic-anisotropic (EAP) approach was introduced by parameterising the anisotropy of the ice stress through interactions of diamond-shaped floes (e.g. Tsamados et al., 2013; Wilchinsky and Feltham, 2004). The free parameters

of the VP rheology have been estimated in various traditional sensitivity experiments (e.g. Panteleev et al., 2020, 2023), and their values are generally considered fixed by the community today.

A new branch of brittle rheologies has been proposed and extended by Girard et al. (2011), Dansereau et al. (2016), and 30 Ólason et al. (2022), with the latest version, the brittle Bingham-Maxwell rheology (BBM) implemented and used in the next generation sea-ice model, neXtSIM (e.g. Rampal et al., 2016, 2019). NeXtSIM, with the BBM rheology, has already been used in several scientific studies (e.g. Boutin et al., 2022, 2023; Korosov et al., 2023; Regan et al., 2023) and is used for operational sea-ice forecasts (Williams et al., 2021), and BBM has been implemented in SI3, the sea-ice component of the NEMO model (Brodeau et al., 2024). However, the free parameters of BBM have only been briefly explored, and their range and relation to 35 other model components and parameters remain unclear.

The BBM rheology, like the other brittle rheologies, is a damage-propagation model. It parameterises the density of fractures (the mechanical weakness of sea ice) at the sub-grid scale with a scalar damage variable. In this framework, undamaged ice is fully elastic, and damage increases when the local stresses reach the Mohr-Coulomb failure criterion. An increase in damage results in a decrease in elasticity, simulating the fracturing of the ice. Once fractured, the ice can also deform viscously, 40 simulating the permanent deformation of fractured ice. This permanent viscous deformation is limited in convergence by resistance to ridge formation, which is also accounted for by the BBM rheology.

As pointed out in Ólason et al. (2022), BBM has many parameters, some well-defined constants and some poorly constrained. These parameters strongly and nonlinearly impact the patterns of sea ice drift and deformation simulated by the model. Visually, the differences between observed and simulated deformation fields can guide the selection of a model parameter value. Still, 45 such manual tuning can become complicated when several parameters must be considered. This work aims to develop a set of metrics for quantitative comparison of the simulated and observed sea ice deformation fields and to use these metrics for tuning BBM parameters utilising a deep learning approach.

## 2 A brief introduction of BBM rheology

The constitutive model of BBM consists of a parallel dashpot and a friction element, connected in series with a spring (see 50 Figure A1). The spring represents elastic ice deformation, the dashpot viscous deformation when the ice is fractured, and the friction element represents the resistance of broken ice to ridge formation. In a simple 1D case, these regimes can be summarised as follows (with  $\sigma$ ,  $\sigma_E$  and  $\sigma_v$  denoting total, elastic and viscous internal stresses, and  $\varepsilon$ ,  $\varepsilon_E$  and  $\varepsilon_v$ , total, elastic and viscous deformations). Note that due to the serial connectivity, the elastic stress always equals the total stress  $\sigma_E = \sigma$ .

- Sea ice is undamaged, viscous stress is zero, and total deformation is fully reversible (elastic):  $d = 0$ ,  $\sigma_v = 0$ ,  $\varepsilon = \varepsilon_E$ , 55 where damage is a single scalar to parametrise the fracture density at the sub-grid scale. The damage value is altered whenever the local stress exceeds the Mohr-Coulomb failure criterion.
- Ice is damaged and diverging; the friction element is inactive and, therefore, the viscous stress equals the elastic and the total stress. Deformation is both elastic and viscous:  $d > 0$ ,  $\sigma > 0$ ,  $\sigma_v = \sigma_E = \sigma$ ,  $\varepsilon = \varepsilon_E + \varepsilon_v$

– Ice is damaged and converging with weak internal stress, the friction element is active, viscous stress is zero, and all deformations are elastic.  $d > 0$ ,  $P_{\max} < \sigma < 0$ ,  $\sigma_v = 0$ ;  $\varepsilon = \varepsilon_E$ , where  $P_{\max}$  is a compressive ice strength threshold that separates elastic from elastic and stress-dissipative behaviour of damaged sea ice.

– Ice is damaged and converging with strong internal stresses, the friction element is inactive and, therefore, the viscous stress is equal to the elastic and the total stress, deformation is both elastic and viscous:  $d > 0$ ,  $\sigma < P_{\max}$ ,  $\sigma_v = \sigma - P_{\max}$ ;  $\varepsilon = \varepsilon_E + \varepsilon_v$

65 Accounting for two components of the internal stress tensor (normal stress,  $\sigma_N$  and tangent stress,  $\tau$ ), we can generalise the equation for the viscous stress as follows:

$$\sigma_v = (1 + \tilde{P})\sigma, \quad (1a)$$

$$\tilde{P} = \begin{cases} \frac{P_{\max}}{\sigma_N} & \text{for } \sigma_N < -P_{\max}, \\ -1 & \text{for } -P_{\max} < \sigma_N < 0, \\ 0 & \text{for } \sigma_N > 0. \end{cases} \quad (1b)$$

where the threshold  $P_{\max}$  separates the elastic and visco-elastic regimes and can be computed following the results of Hopkins 70 (1998) and Hibler (1979):

$$P_{\max} = P_0 \left( \frac{h}{h_0} \right)^H e^{C(1-A)}, \quad (2)$$

where  $h$  is sea ice thickness,  $h_0 = 1$  m is a constant reference thickness,  $H = 3/2$  is the exponent of the compression factor,  $P_0$  is a constant reference stress,  $C < 0$  is compaction parameter and  $A$  is ice concentration.

The time derivative of total stress (see details in Olason et al., 2022) is

$$75 \quad \dot{\sigma} = E \mathbf{K} : \dot{\varepsilon} - \frac{\sigma}{\lambda} \left( 1 + \tilde{P} + \frac{\lambda \dot{d}}{1 - d} \right), \quad (3)$$

where elasticity is a function of damage and concentration:

$$E = E_0(1 - d)e^{C(1-A)}, \quad (4)$$

$\mathbf{K} : \dot{\varepsilon}$  is the stiffness tensor operation:

$$\begin{pmatrix} (\mathbf{K} : \dot{\varepsilon})_{11} \\ (\mathbf{K} : \dot{\varepsilon})_{22} \\ (\mathbf{K} : \dot{\varepsilon})_{12} \end{pmatrix} = \frac{1}{1 - \nu^2} \begin{pmatrix} 1 & \nu & 0 \\ \nu & 1 & 0 \\ 0 & 0 & 1 - \nu \end{pmatrix} \begin{pmatrix} \dot{\varepsilon}_{11} \\ \dot{\varepsilon}_{22} \\ \dot{\varepsilon}_{12} \end{pmatrix}, \quad (5)$$

80  $\lambda$  is the viscous relaxation time:

$$\lambda = \lambda_0(1 - d)^{\alpha-1}, \quad (6)$$

**Table 1.** The default and optimised (see Section 5.4) parameters of BBM rheology.

Parameter	Symbol	Default value	Optimal value
Undamaged elasticity	$E_0$	$5.96 \times 10^8$ Pa	
Undamaged viscous relaxation time	$\lambda_0$	$1 \times 10^7$ s	
Reference thickness	$h_0$	1 m	
Damage parameter	$\alpha$	5	
Compaction parameter	$C$	-28	
Scaling parameter for compressive strength	$P_0$	10 kPa	5.1 kPa
Cohesion at the reference scale	$c_{\text{ref}}$	1 MPa	1.2 MPa
Poisson's ratio	$\nu$	1/3	
Internal friction angle tangent	$\mu$	0.7	0.7
Exponent of compression factor	$H$	3/2	
Ice-atmosphere drag coefficient	$C_A$	$2.0 \times 10^{-3}$	$2.28 \times 10^{-3}$

with  $E_0$  (undamaged elasticity),  $\nu$  (Poisson's ratio),  $\lambda_0$  (undamaged viscous relaxation time), and  $\alpha > 0$  is a constant.

Damaging occurs in the BBM rheology whenever the simulated stress in a grid cell or element is outside the failure envelope, or yield curve. The failure envelope of the BBM rheology is the Mohr-Coulomb criterion:

$$85 \quad \tau = \mu \sigma_N + c, \quad (7)$$

where  $\mu$  is the internal friction coefficient and  $c$  is the cohesion. Following Bouillon and Rampal (2015), we let the cohesion scale with model resolution as

$$c \sim c_{\text{ref}} \sqrt{\frac{l_{\text{ref}}}{\Delta x}}, \quad (8)$$

where  $\Delta x$  is the distance between model node points, and  $c_{\text{ref}}$  is the cohesion at the reference length scale,  $l_{\text{ref}} = 10$  cm, where 90 the cohesion was measured to be of the order of 1 MPa (Schulson et al., 2006).

The aforementioned parameters of the neXtSIM BBM rheology are summarised in Table 1. The ice-atmosphere drag coefficient  $C_A$  is also added to the table (although, strictly speaking, it is not a rheology parameter) because it controls the amount of energy transferred from wind and ocean into sea ice, strongly affects the sea ice drift speed and, correspondingly, sea ice deformation. According to Ólason et al. (2022), such parameters as  $P_0$  and  $c_{\text{ref}}$  require tuning using satellite observations at 95 large spatial and temporal scales. Given that the rheology parameters nonlinearly affect the field of sea ice deformation, a metric based on satellite-derived deformation should be used, and the tuning should capitalise on nonlinear methods, such as deep learning.

### 3 Data

We used the Lagrangian sea ice motion data from the Radarsat Geophysical Processing System (RGPS) (Kwok et al., 2008) 100 for tuning the above rheology parameters. The dataset contains trajectories of virtual buoys tracked using pattern-matching techniques on SAR imagery from Radarsat-2. The buoys are initialised by RGPSS in mid-December in the western Arctic on a regular grid with 10 km spacing on individual SAR images. The position of each virtual buoy is tracked from one image to another overlapping image during the entire winter season (December – May). The trajectory is terminated if a virtual buoy cannot be tracked due to a loss of similarity between SAR images or the absence of images. New virtual buoys are initialised 105 in the regions with low density of the tracked buoys that appear due to sea ice divergence or disappearance of older buoys. The average time between overlapping Radarsat-2 image acquisitions is three days but may vary from 0.5 to 10 days. Therefore, the timing of virtual buoy positions is highly heterogeneous, even for neighbour trajectories (see Section A for details).

### 4 Methodology

#### 4.1 Overview of the parameter tuning algorithm

110 In our approach, we compute a set of descriptors that characterise patterns in the fields of observed and simulated sea ice deformation. Since the correlation between the descriptors and model parameters is weak (see Fig. 6), we could not use linear regression-based methods (e.g., Ensemble Kalman filter; Massonnet et al., 2014; Zhang et al., 2021; Chen et al., 2024) and chose a deep learning (DL) approach instead. In our DL approach for tuning the neXtSIM parameter values, we train a neural network based on the modelling results and apply it to actual observations. The inputs for the neural network are the descriptors 115 of the sea ice deformation, and the target is a value of a rheological parameter.

The algorithm for DL parameter tuning can be summarised as follows:

1. We choose the neXtSIM rheology parameters for tuning and perturb their values to generate an ensemble. Let  $\phi_{m,n}$  denote the  $m$ -th parameter for the  $n$ -th member of the ensemble, then  $\phi_m$  denotes a vector of the  $m$ -th parameter for all members.
2. An ensemble of neXtSIM instances is run with the same forcings but with different rheology parameters:

$$\tilde{\mathbf{x}}_{n,t+1} = \mathcal{M}(t, \tilde{\mathbf{x}}_{n,t}; \phi_n), \quad (9)$$

where  $\tilde{\mathbf{x}}$  is the sea ice model state (e.g., sea ice concentration, thickness, drift, etc.),  $\mathcal{M}$  is neXtSIM model, and  $t$  is time.

3. Let  $\mathbf{x}$  denote only one model variable: sea ice drift. Then  $\mathcal{H}$  denotes the operator for computing a sea ice deformation field and a quantitative characterisation of ice deformation pattern  $\mathbf{y}$ :

$$\mathbf{y}_{n,t} = \mathcal{H}(\mathbf{x}_{n,t}). \quad (10)$$

The size of  $\mathbf{y}_{n,t}$  is much smaller than the ice deformation field. For example, a daily deformation field containing  $\sim 10^{10}$  sea ice deformation values can be characterised by a vector with  $\sim 50$  values.

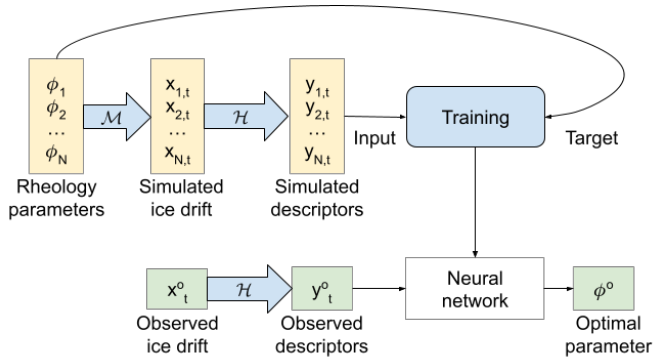


**Figure 1.** Scheme of ML-based tuning of neXtSIM parameters. Blue arrows denote operations with data. Yellow squares denote modelling data. Green squares denote observations. The operators  $\mathcal{M}$  and  $\mathcal{H}$  denote, correspondingly, neXtSIM simulations and computation of sea ice deformation descriptors.

4. Let  $\mathbf{y}$  denote a set of  $\mathbf{y}_{n,t}$  vectors from all members and all time steps. Hereafter,  $\mathbf{y}$  is called deformation pattern  
 130 descriptors, or simply, descriptors. A neural network  $\mathcal{N}$  is trained (operator  $\mathcal{T}$ ) with the deformation pattern descriptors  
 $(\mathbf{y})$  as input and the rheology parameters ( $\phi_m$ ) as the target:

$$\mathcal{N}_m = \mathcal{T}(\mathbf{y}, \phi_m). \quad (11)$$

5. Deformation fields and deformation pattern descriptors are computed from the observed sea ice drift  $\mathbf{x}^o$  for each time  
 step  $t$ :

$$\mathbf{y}_t^o = \mathcal{H}(\mathbf{x}_t^o). \quad (12)$$

135 6. The neural network is applied to the deformation pattern descriptors computed from the observed ice drift, and averaging  
 $(\langle \rangle)$  is applied for computing the optimal value of a neXtSIM parameter:

$$\begin{aligned} \phi_{m,t}^o &= \mathcal{N}_m(\mathbf{y}_t^o) \\ \phi_m^o &= \langle \phi_{m,t}^o \rangle. \end{aligned} \quad (13)$$

All these steps are described in detail below.

## 4.2 Running an ensemble of neXtSIM instances

140 We ran two ensembles with neXtSIM instances. In the first experiment, the ensemble consisted of 50 members and the values  
 of four parameters were perturbed using Latin Hypercube (McKay et al., 1979):  $P_0$ ,  $c_{\text{ref}}$ ,  $\nu$  and  $\mu$ . In the second experiment with  
 70 members, the following parameters were perturbed with the same method:  $P_0$ ,  $c_{\text{ref}}$ ,  $H$ ,  $C$  and  $C_A$ . The  $H$  and  $C$  parameters  
 were added because they control the influence of sea ice thickness on  $P_{\max}$ . See the ranges of the perturbed parameters in  
 Table 2.

**Table 2.** Ranges of parameters perturbed in two experiments.

Experiment	Parameter	Symbol	Min	Max
1	Scaling parameter for compressive strength	$P_0$	0	20 kPa
	Cohesion at the reference scale	$c_{\text{ref}}$	0.5	3 MPa
	Poisson's ratio	$\nu$	0.27	0.33
	Internal friction angle tangent	$\mu$	0.55	0.75
2	Scaling parameter for compressive strength	$P_0$	0	15 kPa
	Cohesion at the reference scale	$c_{\text{ref}}$	0.2	2 MPa
	Exponent of compression factor	$H$	0.5	2.5
	Compaction parameter	$C$	-50	-5
	Ice-atmosphere drag coefficient	$C_A$	0.001	0.003

145 NeXtSIM instances were run at 10 km resolution mesh, covering the central Arctic Ocean. Ocean forcing from TOPAZ4 reanalysis (Sakov et al., 2012) and atmosphere forcing from ERA5 reanalysis (Hersbach et al., 2020) were used. NeXtSIM exports snapshot outputs every hour with coordinates and connectivity of the nodes of the triangular mesh and model variables for each mesh element, including ice concentration, thickness, etc. End-to-end indexing of the model nodes allows the identification of similar nodes on two snapshots and the computation of the displacement of the node, i.e., the simulated sea ice  
150 drift.

### 4.3 Preprocessing of neXtSIM data

155 To ensure comparability of sea ice drift and deformation from RGPS and neXtSIM, we subsample the model mesh using the mesh of satellite observations. First, for a given set of virtual RGPS buoys that have the same starting time and ending time (i.e., a single pair of SAR images is used for ice drift computation for these buoys), two model snapshots with the closest simulation time are selected from the neXtSIM outputs. Next, only the neXtSIM nodes near the RGPS nodes are selected on the first snapshot, and the corresponding nodes are chosen on the second snapshot (see Figure A3 for an example). Nodes may disappear during simulation, or new nodes appear due to convergence/divergence and consequent remeshing. In that case, a new Delaunay triangulation connectivity is computed between the nodes existing on the first and the second snapshots. Further drift, deformation, and descriptor calculations are performed on subsets of trajectories (same for RGPS or neXtSIM) with the  
160 same start and end time. They are somewhat limited in space (by the intersection area of two SAR images).

### 4.4 Computing the descriptors of the sea ice deformation

We compute the divergence and shear components of the deformation tensor and the total deformation rates using a standard method of contour integrals of velocity (Kwok, 2006) for each element of the mesh subset mentioned above. The following descriptors of the total deformation field are computed from each subset as described in the subsections below:

165 1. Structure-function from the spatial scaling analysis

2. Image anisotropy at different spatial scales

3. Haralick texture features at different spatial scales

4. Length, density and angle of intersection of linear kinematic features (LKF)

5. Mean and 90th percentile of ice deformation values

170 **4.4.1 Spatial scaling analysis**

As described in Ólason et al. (2022), the deformation is computed at different spatial scales by iterative coarse-graining (Marsan and Weiss, 2010). First, the deformation is calculated on the native resolution of RGPS and neXtSIM (which are very similar). Next, some nodes are randomly removed, the remaining node positions are triangulated, and deformation is computed again. The last step is repeated several times until at least three nodes remain in the subset. Information about the area of the element used for computing deformation is preserved. This iterative procedure is repeated several times, starting from the initial deformation field to collect sufficient deformation observations computed at different spatial scales.

175 The spatial scale  $L$  is linked with the statistical moments  $Q$  of the total deformation probability density function using the following equation:

$$L_{lg} = \alpha_N + \beta_N Q_{lg}^N, \quad (14)$$

180 where  $\alpha$  and  $\beta$  are coefficients found using the least squares method,  $N$  is the statistical moment order, and the subscript  $lg$  indicates logarithmic space. The  $N$ -th statistical moment is computed as  $Q_{lg}^N = \langle \log_{10}((\varepsilon - \hat{\varepsilon})^N) \rangle$ , where  $\hat{\varepsilon}$  is mean total deformation and  $\langle \rangle$  denotes averaging.

185 Coarse graining is performed on each deformation subset (see Section 3.3). Still, the  $\alpha$  and  $\beta$  coefficients are computed using deformation values (and corresponding spatial scales) from all image pairs acquired within three days. Hereafter, the offset and scale of the 1<sup>st</sup> statistical moment is denoted `mom_1o` and `mom_1s`, and so on (see Table 3).

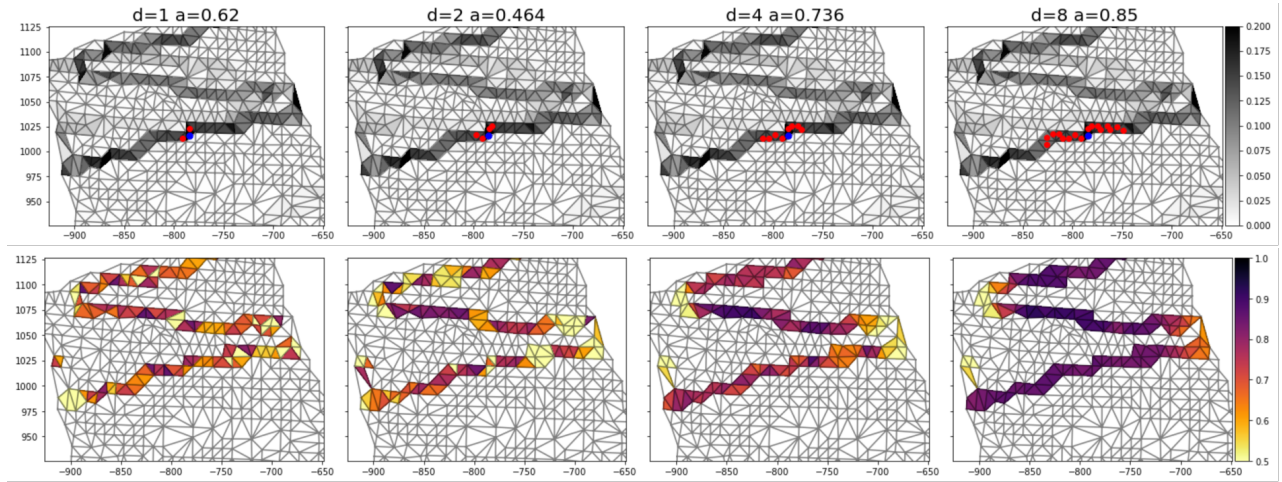
**4.4.2 Image anisotropy**

Image anisotropy  $a_I$  characterises localisation of image intensity in a linear feature (Lehoucq et al., 2015). Anisotropy is high (up to 1) for images of bright, narrow, long lines and is low (down to 0) for images with darker, shorter or thicker lines. We compute the image anisotropy as:

$$190 a_I = 1 - \sqrt{\frac{\lambda_1}{\lambda_2}} \quad (15)$$

where  $\lambda_1$ , and  $\lambda_2$  are the eigenvalues of the inertia matrix  $\mathbf{P}$ :

$$\mathbf{P} = \sum_{box} \begin{pmatrix} X^2 & XY \\ XY & Y^2 \end{pmatrix} I \quad (16)$$



**Figure 2.** Computation of image anisotropy on a mesh subset. The upper row shows a mesh subset with values of ice deformation ( $d^{-1}$ ), and the lower row - values of anisotropy computed at different spatial scales. The blue dot on the upper row shows the location of an arbitrary element for which anisotropy is computed, and the red dots show the neighbours from which the deformation and coordinates are collected.

where  $X$  and  $Y$  are coordinates of the pixels of the image with intensities  $I$  (i.e. ice deformation in our case).

In our study, anisotropy is computed on triangular mesh elements as illustrated in Fig. 2. Only elements with deformation 195 above  $0.1 \text{ d}^{-1}$  are used to avoid the impact of noise in sea ice drift and deformation (Dierking et al., 2020). For computing  $a_I$  in a selected element, the nearest neighbour elements are found, and values of deformation and the coordinates of the centres of the elements are used in Eqs. 15 and 16 (see Fig. 2, left column). For larger spatial scales (Fig. 2, 2nd, 3rd and 4th columns), values of the deformation and coordinates are collected from the neighbours of the neighbours. After processing a single mesh 200 subset, each element is characterised by a vector of image anisotropy computed at spatial scales of 10, 20, 30, 40 and 50 km. For every three days, a median and 90<sup>th</sup> percentile (P90) of anisotropy from all elements of all mesh subsets are computed for each spatial scale and denoted hereafter as  $a_{50\_00}$ ,  $a_{90\_00}$  and so on (see Table 3).

#### 4.4.3 Texture features

Haralick texture features (TF) are extensively used for quantitative characterisation of image texture in tasks dealing with image segmentation (Haralick et al., 1973; Zakhvatkina et al., 2017; Park et al., 2019). A grey-level co-occurrence matrix (GLCM) 205 is computed at the first stage of the texture analysis. GLCM is a 2D distribution of the probability of a pixel value and its neighbour value. The neighbours can be selected at varying orientations and distances from the central pixel. At the second stage of texture analysis, several simple algebraic formulas are applied to the GLCM to compute statistical moments of the distribution (e.g., mean, standard deviation, kurtosis, etc.) and more complex characteristics (energy, entropy, etc.)

In our study, we compute the GLCM from the triangular mesh elements. We accumulate information about an element 210 and all its neighbours at a given distance in all directions in one GLCM. For one-edge distance, we use the values from

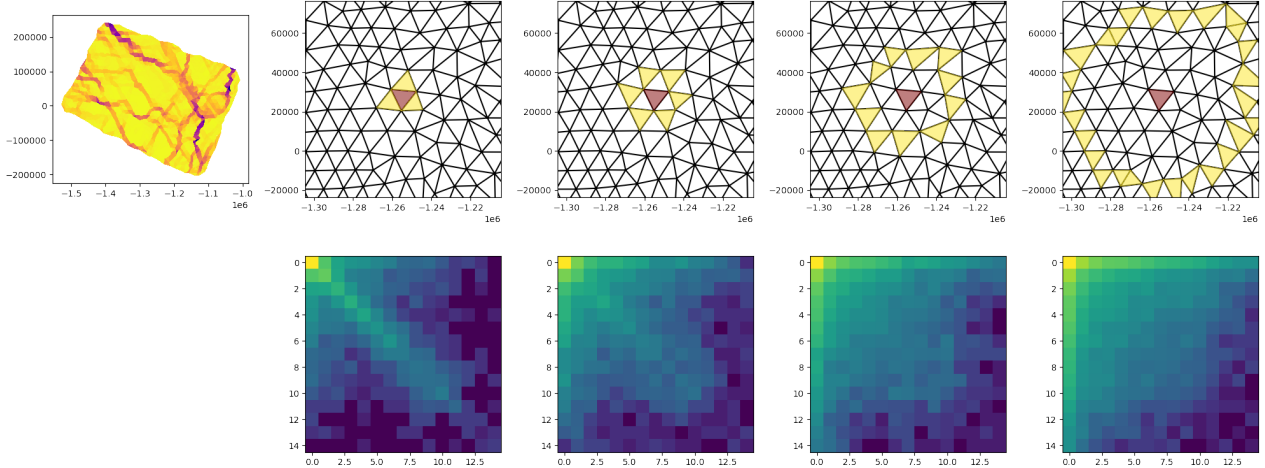


**Figure 3.** Scheme of GLCM computation. The upper left map shows a mesh subset with values of total deformation from neXtSIM. The upper row shows neXtSIM mesh with the central element coloured orange, and the neighbours at the one, two, four, and eight edge distances are coloured yellow. The lower row of images shows corresponding GLCM matrices.

three immediate neighbours; for two–edge distances, we use the values from neighbours of neighbours (excluding the central element and duplication), and so on, as shown in Fig. 3. We populate the GLCM matrix with data from all elements from all mesh subsets acquired within three days. The following texture features (TFs) are computed at distances of 1, 2, 4, and 8 edges using the `scikit-image` Python library (van der Walt et al., 2014): Dissimilarity, Homogeneity, Angular Second Moment, 215 Energy, Correlation, Contrast. For notation, see Table 3. Zakhvatkina et al. (2017) provides the exact formulas.

#### 4.4.4 LKF intersection angle

Hutter et al. (2019) proposed a method for detecting linear kinematic features (LKFs) on RGPS and model data and several metrics for the characterisation of LKFs. These metrics are successfully applied to evaluate sea ice models in a large intercomparison experiment (Hutter and Losch, 2020). In our work, we rasterised the 3-day deformation maps on 12.5 km resolution 220 grids and applied the LKF detection method of Hutter et al. (2019). The number of LKFs, average length of LKFs, and average intersection angle of conjugate faults were used as the descriptors (see Table 3 for notations).

In addition to the descriptors listed above, the median and P90 of divergence, convergence and shear were computed for each of the three days. Thus, a vector of descriptors constituted 49 values: median and P90 of deformation; median and P90 of image anisotropy computed at five spatial scales; 6 texture features at four distances; slopes and offsets of 3 statistical moments; 225 length, number and intersection of LKFs. Table 3 shows the notation used hereafter in detail. Such vectors were generated from neXtSIM simulations for each day (using a sliding window of 3 days) from 5 December 2006 to 11 April 2007 for the first experiment and from 5 December 2006 to 15 May 2007 for the second experiment. Therefore, we had  $127 \times 50 = 6350$  and  $161 \times 70 = 11270$  vectors for training the ML model in the first and the second experiments.

**Table 3.** Descriptors notation.

Description	Notation
Divergence, Convergence and Shear median and P90	div_50, div_90, cnv_50, cnv_90, she_50, she_90
Anisotropy median at 10, 20, 30, 40 and 50 km spatial scale	a50_00, a50_05, a50_10, a50_15, a50_20
Anisotropy P90 at 10, 20, 30, 40 and 50 km spatial scale	a90_00, a90_05, a90_10, a90_15, a90_20
Dissimilarity TF at a distance of 1, 2, 4, 8 pix	dis_01, dis_02, dis_04, dis_05
Homogeneity TF at a distance of 1, 2, 4, 8 pix	hom_01, hom_02, hom_04, hom_05
Angular Second Moment TF at a distance of 1, 2, 4, 8 pix	asm_01, asm_02, asm_04, asm_05
Energy TF at a distance of 1, 2, 4, 8 pix	ene_01, ene_02, ene_04, ene_05
Correlation TF at a distance of 1, 2, 4, 8 pix	cor_01, cor_02, cor_04, cor_05
Contrast TF at distances of 1, 2, 4, 8 pix	con_01, con_02, con_04, con_05
1 <sup>st</sup> , 2 <sup>nd</sup> and 3 <sup>rd</sup> statistical moment slope and offset	mom_1s, mom_2s, mom_3s, mom_1o, mom_2o, mom_3o
Average LKF intersection angle, length and number	1kf_an, 1kf_ln, 1kf_no

#### 4.5 Selection of usable descriptors

230 We test the applicability of these descriptors in two steps: comparison of PDFs for descriptors from RGPS and neXtSIM on the one hand and using an autoencoder on the other. In the first step, we scale the values of descriptors from RGPS using the mean and standard deviation of the values from neXtSIM:  $y_s = (y_o - \mu)/\sigma$ , where  $y_o$  are all descriptors from RGPS,  $\mu$  and  $\sigma$  are mean and standard deviation for all descriptors from neXtSIM.

235 The mean and standard deviation of the scaled descriptors are analysed, and only the descriptors with scaled standard deviation below 3 remain for further use. Six descriptors computed from RGPS data have significantly different values from the neXtSIM descriptors and are expected to mislead the training.

240 We trained an autoencoder (Hinton and Salakhutdinov, 2006; Vincent et al., 2008) with dense layers with 32, 16, 8, 16, and 32 neurons on the down-selected descriptors from neXtSIM. Due to the bottleneck, the autoencoder acts as a nonlinear principal component analysis. It can be used for anomaly detection either in the input features (Hinton and Salakhutdinov, 2006) or in input records (Vincent et al., 2008). We applied the autoencoder to the down-selected neXtSIM and RGPS descriptors and computed the root mean square difference (RMSD) between the input vector and the autoencoder output for neXtSIM and RGPS. We excluded seven descriptors with high RMSE in RGPS data from further processing as anomalous compared to neXtSIM training data.

#### 4.6 Training of machine learning algorithms

245 We trained two types of ML models with the values of deformation pattern descriptors on input and a single value of a neXtSIM parameter as a target: a linear regression model (LR) and a deep neural network (DNN). For both models, we split the dataset from neXtSIM into two parts (85:15) for training and validation. Training and validation data are taken from different months

selected randomly. The models are trained on neXtSIM data and then applied to all RGPS descriptors. We repeated this procedure ten times with a new random permutation and averaged the inference results on RGPS from each repetition. The 250 Eqs. 11 and 13 can be rewritten as follows with  $i$  being the index of repetition:

$$\mathcal{N}_{m,i} = \mathcal{T}(\mathbf{y}_i, \phi_{m,i}), \quad (17a)$$

$$\phi_{m,t,i}^o = \mathcal{N}_{m,i}(\mathbf{y}_t^o), \quad (17b)$$

$$\phi_m^o = \langle \phi_{m,t,i}^o \rangle \quad (17c)$$

The LR model can be formulated as:

$$255 \quad \phi_p = A_p Y, \quad (18)$$

where  $\phi_p$  is the vector of the  $p$ -th model parameter for all 3-day periods,  $Y$  is a matrix with down-selected descriptors for all periods, and  $A_p$  is a matrix with linear regression coefficients for that model parameter. Values in  $A_p$  are found using the least squares method. The LR model does not require a split into training/validation datasets. However, only the training dataset was compared with the DNN results.

260 The DNN model contains three hidden dense layers with 32, 16, and 8 fully connected neurons. We found this architecture optimal in a simple hyperparameter tuning experiment. The hidden layers use the rectified linear units (ReLU) activation function, and the output layer uses linear activation. We trained the DNN with the Adam optimiser (Kingma and Ba, 2017), and the validation loss (computed as absolute error) decreased.

## 5 Results and discussions

### 265 5.1 Sea ice deformation fields from neXtSIM

Ólason et al. (2022) identified  $P_0$  and  $c_{\text{ref}}$  as two parameters of their rheology, which are poorly constrained and have a substantial visual impact on the deformation fields. Fig. 4 compares total sea ice deformation derived from RGPS (first column), and neXtSIM runs from the first experiments with the highest and lowest values of  $P_0$  and  $c_{\text{ref}}$ . Three dates were chosen for Fig. 4 in 2007 with low (15 February), moderate (25 January) and high (3 February) deformation events. These maps illustrate that 270 both parameters significantly affect the pattern of sea ice deformation, but their influence is manifested differently. For example, the increase of  $P_0$  results in broader and longer LKFs with higher deformation rates. These pronounced LKFs surround quite large floes; the background deformation remains relatively low. The increase of  $c_{\text{ref}}$  seems to affect the background deformation more — at the lowest  $c_{\text{ref}}$  value, the deformation between the main LKFs is mostly zero, and it increases with higher  $c_{\text{ref}}$  to become almost spatially homogeneous. Visually, it is hard to say which of these maps better matches the RGPS data, but 275 we can use the similarity of deformation descriptors in PDFs as the metric. Nevertheless, optimisation of multiple rheology parameters is required to find the best match.

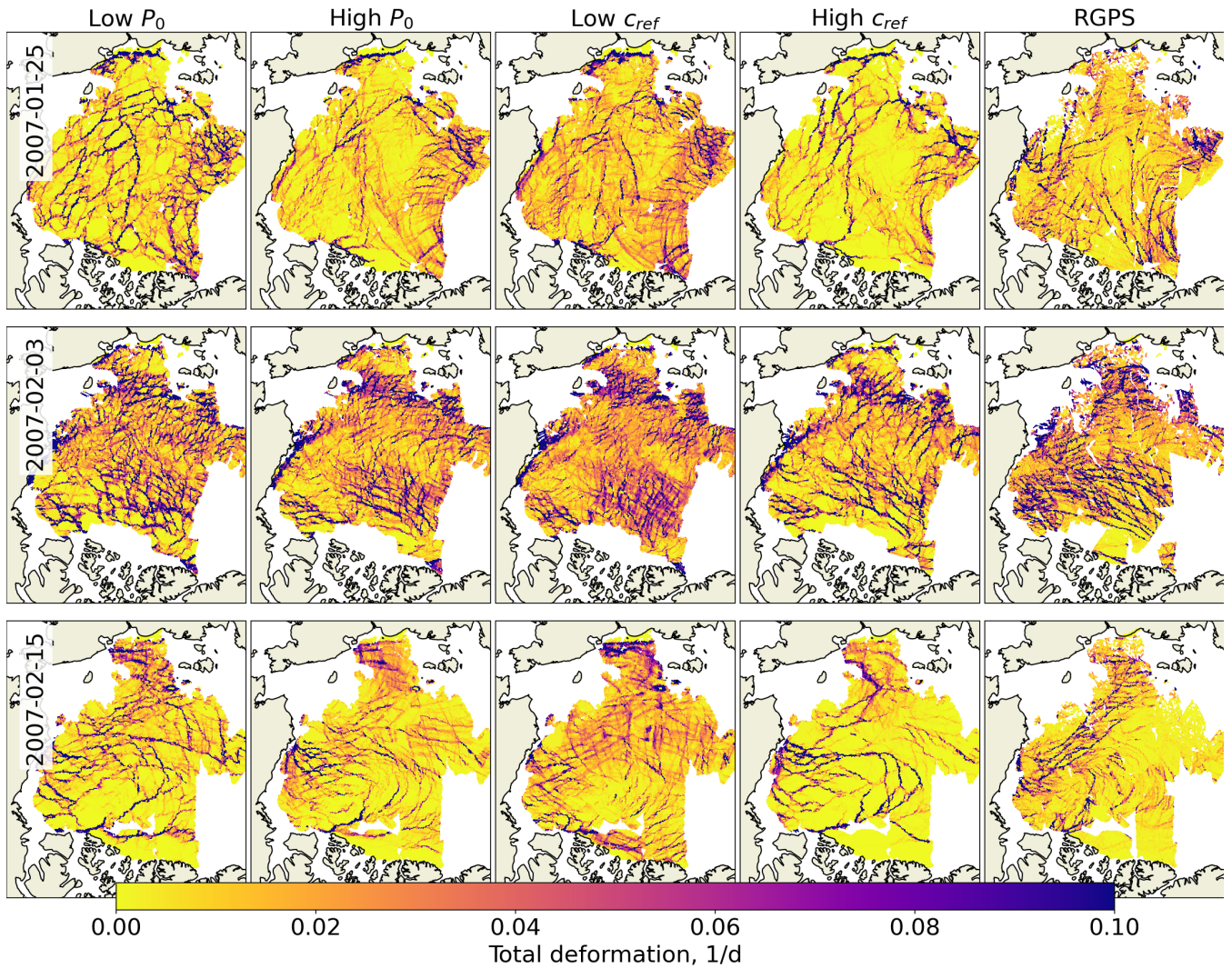


**Figure 4.** Maps of total deformation from RGPS and neXtSIM for three selected dates representing low, moderate and strong deformation events. Each map represents a three-day mosaic, i.e., the deformation is derived from pairs of Radarsat-1 images (and corresponding neXtSIM snapshots) accumulated over three days starting from the indicated date.

## 5.2 Deformation pattern descriptors

Figure 5 shows the PDFs of the deformation pattern descriptors computed from RGP5 and the first neXtSIM experiment.

Comparison of the PDFs from all neXtSIM runs (blue shaded area) with the PDFs from the run with the lowest (orange line) or the highest (green line)  $P_0$  value illustrates that some descriptors (e.g., a50\_00, a90\_05, hom\_02, con\_01-08, etc.) are strongly affected by  $P_0$  — their PDF peaks are distinctly different. Other descriptors (e.g., ASM\_01-08, a50\_10, etc.) have very similar PDFs without regard for the  $P_0$  parameter. See Figure A4 with PDFs of all deformation descriptors for reference.

The PDF of most RGP5-derived descriptors lies well within the range of neXtSIM-derived descriptors and peaks between the highest and lowest  $P_0$  PDFs (e.g., a90\_05, dis\_04, mom\_30, etc.) suggesting that we can use these descriptors for parameter tuning. Some RGP5 descriptors, however, show a completely different distribution (e.g., hom\_08, cor\_08, etc.), probably due to sensitivity to noise in observations. Such descriptors are not usable for parameter training and are excluded as described in section 4.5.

Figure 6 shows the correlation of all descriptors with the values of all parameters from the first experiment. The correlations are generally relatively low, except for  $c_{ref}$ , which correlates with she\_50 and cor\_01 above 0.35. Results from the second experiment are pretty similar.

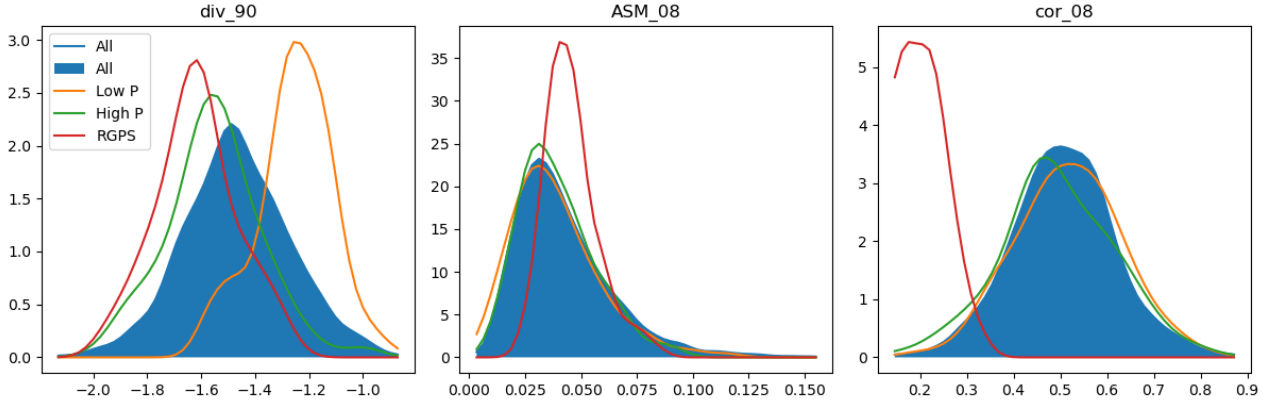
Figure 7 presents the mean and standard deviation of the RGP5-derived descriptors normalised by the mean and standard deviation of the neXtSIM descriptors. We use it at the first step of evaluating usability and downselecting the descriptors. Only 43 descriptors computed from RGP5 data show the relative mean value between -1.5 and 1.5 standard deviations of the neXtSIM descriptors. We exclude the following six descriptors from further processing: cor\_08, a50\_08, cor\_01, ene\_08, dis\_08, hom\_08. The standard deviation of the RGP5 descriptor a90\_00 is very large compared to the neXtSIM due to noise in the RGP5 observations of ice drift and deformation (see Figure 3, left panel).

Fig. 8 compares root mean square difference (RMSD) between input and predictions of the autoencoder trained on normalised neXtSIM data and applied to neXtSIM and RGP5 descriptors. The RMSD of neXtSIM — derived descriptors is below one, showing that even a relatively shallow autoencoder (five layers with eight neurons in the bottleneck) can reproduce the variability of the descriptors well. When the same autoencoder is applied to the RGP5 data, some of the descriptors (cnv\_90, con\_08, lkf\_ln, lkf\_no, a90\_20, lkf\_an, and a90\_00) have RMSD higher than the maximum neXtSIM RMSD. High RMSD indicates abnormal values, and we exclude the corresponding descriptors from further training.

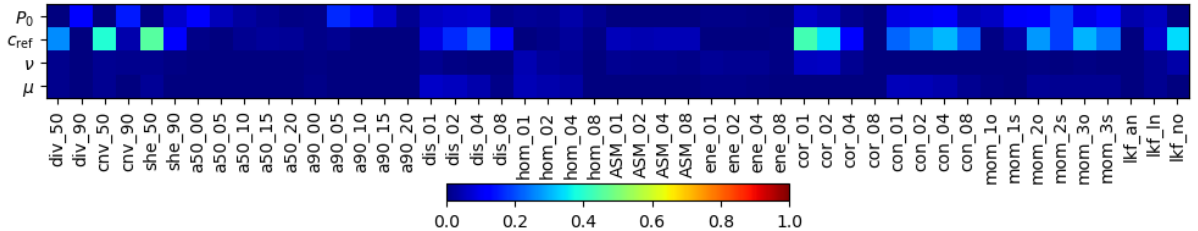
## 5.3 Training and inference of ML models

Fig. 9 shows the DNN training results for the first (upper row) and the second (lower row) experiments (see also Table 4).

These scatterplots compare the actual and the predicted neXtSIM parameters from the test dataset from all ten repetitions. In the first experiment, the DNN derives only the  $P_0$  and  $c_{ref}$  with sufficient accuracy (correlation is 0.75 and 0.88, respectively). In the second experiment, the accuracy of  $P_0$  retrieval is somewhat lower ( $r = 0.61$ ), while the accuracy of  $c_{ref}$  and  $C_A$  retrieval is high (correlation is 0.83 and 0.75, respectively). The DNN does not show any skill in retrieving  $\nu$  or  $H$  parameters, and the



**Figure 5.** PDFs of few deformation descriptors for RGPS (red), all neXtSIM runs (blue), and runs with lowest (orange) or highest values of  $P_0$ . The descriptor  $\text{div}_{90}$  is promising as it shows strong sensitivity to  $P_0$  parameter, and the RGPS values vary within a similar range. The descriptors  $\text{ASM}_08$  and  $\text{cor}_08$  are less usable as they are either not sensitive to  $P_0$  (i.e.,  $\text{ASM}_08$ ) or RGPS values are out of the training range (i.e.,  $\text{cor}_08$ ).



**Figure 6.** Correlations between four parameters of the first experiment and the deformation descriptors.

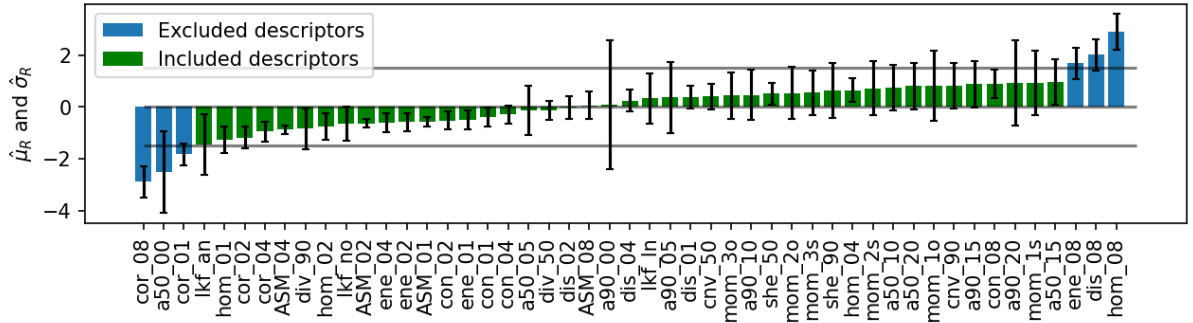


**Figure 7.** Relative values of the mean (shown by bar height) and standard deviation (shown by error bars) of descriptors computed from RGPS data. The blue colour shows the excluded descriptors.

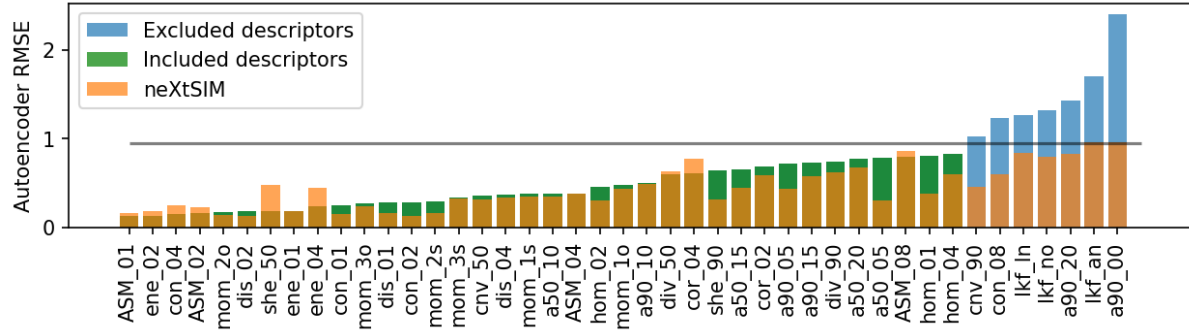


**Figure 8.** RMSD between input and output of the autoencoder trained on neXtSIM data and applied to neXtSIM (orange) and RGP (blue or green). The blue colour shows RGP descriptors excluded from further analysis.

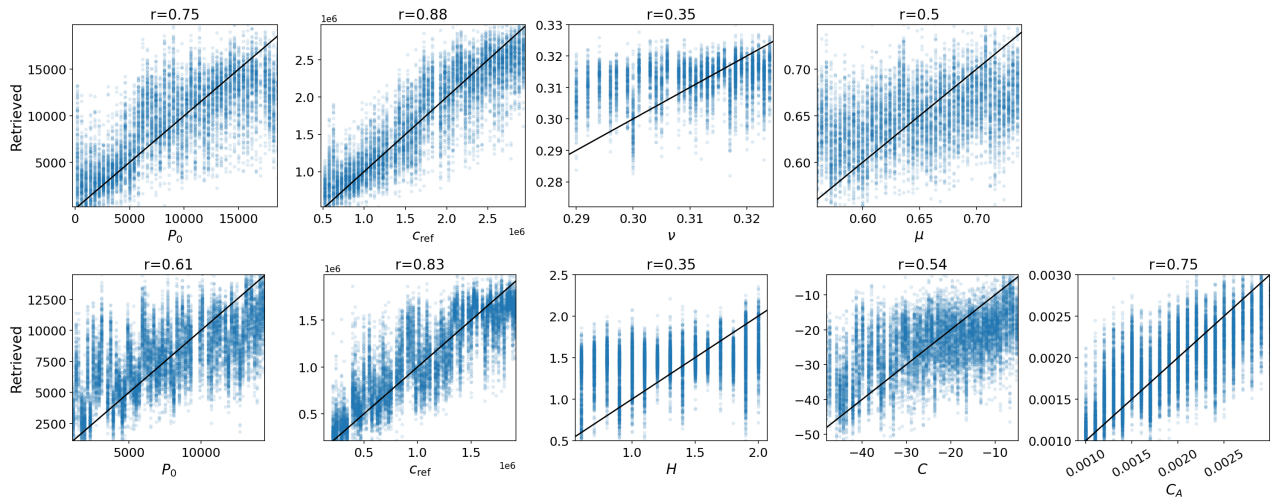


**Figure 9.** Comparison of the actual neXtSIM parameters (X-axis) and the retrievals by the DNN. The upper row shows results from the first experiment, and the lower — the second one. The black lines show a 1:1 relation.

accuracy of retrieving  $\mu$  and  $C$  is somewhat higher for a short range of values. Still, overall, these four parameters cannot be  
310 derived with the machine learning approach. LR accuracy is lower (see Table 4), and the scatterplots are not shown.

Figure 10 shows PDFs of parameters used for training (blue line) and derived from the RGP data using DNN (orange line) and LR (green line) models in the two experiments mentioned above (upper and lower row). In both experiments, PDFs of  $P_0$  and  $c_{ref}$  parameters have a clear peak at  $\approx 5000$  kPa and  $\approx 1.1$  MPa, correspondingly. Notably, these peaks do not correspond to the centre of the distribution of the parameters used for training (blue line). We can observe similar behaviour for  $\mu$  and  
315  $C_A$  parameters, which also have relatively high retrieval accuracy of testing data. For  $\nu$ ,  $H$ , and  $C$  parameters, the situation is

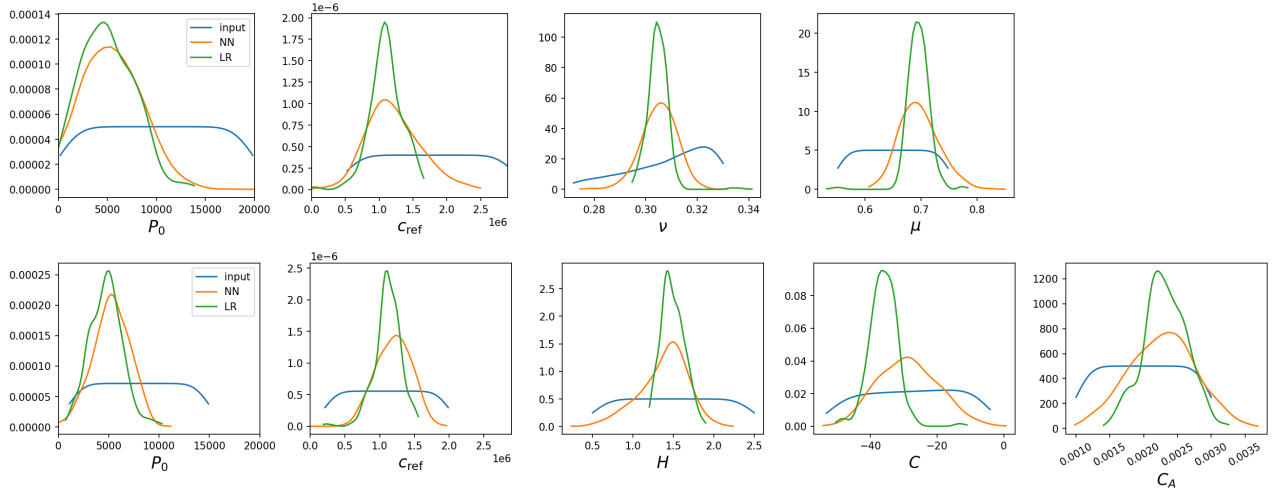


**Figure 10.** PDFs of parameters used for training (blue lines) and derived from RGPS descriptors using DNN (orange) and LR (green). The upper row shows the results from the first experiment, and the lower — the second.

different — the accuracy of the retrievals on the testing data was low, and the retrievals from the RGPS data are centred in the distribution of training values.

#### 5.4 Optimal rheology parameters for neXtSIM

Since the training accuracy was high, the peaks of PDFs of RGPS-derived parameters are pronounced and have offset from the centre of the input data distribution; we can conclude that the values of  $P_0$ ,  $c_{\text{ref}}$ ,  $\mu$  and  $C_A$  parameters derived from RGPS 320 can be used for optimal representation of the deformation patterns by neXtSIM. Table 4 lists the parameter values derived in different experiments and the accuracy of the model training. Note that DNN always has higher accuracy than the LR model.

We ran neXtSIM with the optimal parameter values, and Figure 11 shows a comparison with RGPS for the exact three dates. We can see that the patterns of the divergence and shear fields are very similar for neXtSIM and RGPS concerning the density 325 and orientation of LKFs, the magnitude of deformation, and, overall, the texture of the deformation field, thus confirming that the found parameters are indeed optimal.

We compared the PDFs of the deformation descriptors using the Kholmogorov-Smirnov (KS) test. The KS test is applied to the PDFs of deformation descriptors computed from neXtSIM and RGPS and is averaged over all usable descriptors. The average KS test is the lowest for the neXtSIM run with the optimal parameters (0.41) and is slightly lower than for the default 330 parameters (0.49).

The simulated sea ice drift was validated against the RGPS drift by comparing the velocity vectors of each virtual buoy from RGPS data and the matching node on the neXtSIM mesh. The ice drift root mean square error for the run with optimal parameters is 0.04 m/s, slightly lower than for the run with the default parameters (0.05 m/s).

**Table 4.** Average values of neXtSIM parameters derived from RGPS. The optimal values are marked in bold.

Param	Exp	Method	$r$ training	Mean inference
$P_0$	1	LR	0.66	4.88 kPa
$P_0$	1	NN	0.75	<b>5.11 kPa</b>
$c_{\text{ref}}$	1	LR	0.83	1.10 MPa
$c_{\text{ref}}$	1	NN	0.88	<b>1.21 MPa</b>
$\nu$	1	LR	0.36	0.305
$\nu$	1	NN	0.35	0.305
$\mu$	1	LR	0.4	0.70
$\mu$	1	NN	0.5	<b>0.70</b>
$P_0$	2	LR	0.59	4.72 kPa
$P_0$	2	NN	0.61	5.26 kPa
$c_{\text{ref}}$	2	LR	0.78	1.11 MPa
$c_{\text{ref}}$	2	NN	0.83	1.19 MPa
$H$	2	LR	0.3	1.49
$H$	2	NN	0.35	1.38
$C$	2	LR	0.47	-36.1
$C$	2	NN	0.54	-28.7
$C_A$	2	LR	0.69	$2.32 \times 10^{-3}$
$C_A$	2	NN	0.75	<b><math>2.28 \times 10^{-3}</math></b>

Sea ice thickness (SIT) from different runs was compared to the monthly average ice thickness from ICESat-1 in March 335 2007 (Zwally et al., 2014). SIT RMSE is the highest ( $\approx 1.3$  m) for the runs with  $C_{\text{ref}} \approx 0.5$  MPa, but no significant differences between the other runs were found ( $\text{RMSE} \approx 1$  m).

It is interesting to note similarities and differences between the parameters used by Ólason et al. (2022). We note that the values we get for  $\nu$ ,  $\mu$ , and  $H$  are very similar to those Ólason et al. (2022) used. This is to be expected for  $\nu$  and  $\mu$ , which are based on well established values (see, e.g. Weiss and Schulson, 2009; Mellor, 1986). Ólason et al. (2022) chose  $H = 3/2$  340 based on the modelling work of Hopkins (1998), but it is unclear whether this should be valid at the geophysical scale. The accuracy of our estimate for  $H$  is low, but it is reasonably close to  $H = 3/2$  and within the expected range of  $H \in [1, 2]$ .

In terms of the stress balance in the ice,  $C_A$ ,  $P_0$ , and  $c_{\text{ref}}$  are the most important, as they determine the momentum transfer from atmosphere to ice, the resistance to ridging, and the shear strength of the ice, respectively. Interestingly, our estimate of  $C_A$  is higher than the value used by Ólason et al. (2022);  $2.28 \times 10^{-3}$  vs.  $2.0 \times 10^{-3}$ , resulting in more momentum transfer 345 from the atmosphere to the ice. At the same time, both  $P_0$  and  $c_{\text{ref}}$  are lower; 5.11 kPa vs. 10.0 kPa and 1.21 MPa vs. 2.0 MPa, respectively. This results in an overall weaker ice cover compared to the parameters used by Ólason et al. (2022). It would, therefore, be reasonable to expect that our set of parameters would lead to an overestimate of the deformation, but this is not

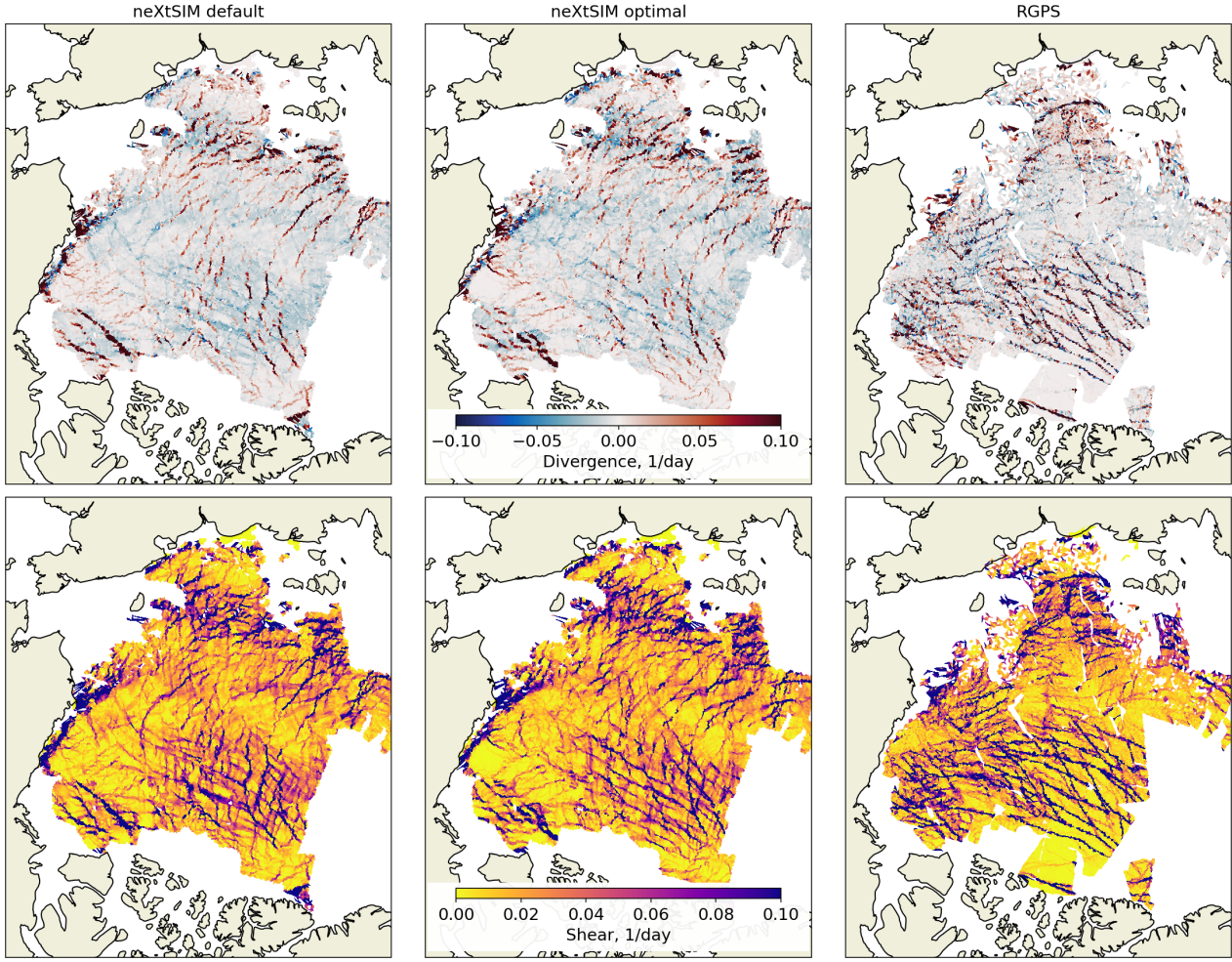


**Figure 11.** Maps of divergence and shear from neXtSIM run with default parameters (left column), optimal parameters (central column) and from RGPS (right column) for 3<sup>rd</sup> February 2007.

the case. This underlines the system's complexity and indicates that there may be multiple local minima in the parameter space, giving reasonable results. For such a system, using a systematic approach which samples the full parameter space - similar to  
350 what we propose here - is extremely beneficial.

### 5.5 Temporal variations of neXtSIM parameter values

The PDFs of parameters presented in Figure 10 are derived from all RGPS descriptors computed in winter 2006–2007. However, we can also apply the ML model trained on neXtSIM data from winter 2006/07 to the RGPS data acquired since 1998. We applied the autoencoder described in Sections 4.5 and 5.3 to the RGPS data from the earlier period to test that the trained ML

355 model has sufficient generalisation skills. We could not detect any significant anomalies in this data. Since the encoder section of the autoencoder has the same architecture as the ML model used for inferring the rheology parameters, we can conclude that the ML model trained on data from winter 2006/07 is general enough to be applied to the earlier RGPS data.

360 Figure 12 shows temporal variations of the derived optimal parameters on daily and inter-annual time scales. To create the latter plot, we computed the descriptors from the RGPS data for 1997–2008 and applied the DNN models trained on neXtSIM data from 2006–2007.

365 On daily time scales, the derived parameters show very high variability, reflecting frequent changes in the pattern of sea ice deformation due to varying atmospheric forcing. The DNN model from the first experiment is more sensitive to these variations and even produces unphysical negative values of  $P_0$  during very high deformation at the beginning of February 2007. Despite substantial variability, the parameters are stable on the annual scale and don't show any significant trends.

370 On the interannual scale, the parameters tend to change;  $P_0$  and  $\mu$  slightly decrease, while  $c_{\text{ref}}$  and  $A_C$  gradually increase. A gradual change in the observed pattern of sea ice deformation can explain this observation. In the 90s, thicker ice had sparser and more pronounced LKFs (see Fig. 4, high  $P_0$  and low  $c_{\text{ref}}$  maps). As ice became thinner, more background deformation appeared, LKFs became denser, and the magnitude of deformation in LKFs slightly decreased (see Fig. 4, low  $P_0$  and high  $c_{\text{ref}}$  maps). The impact of internal friction angle or air drag is not shown in Figure 4, but the mechanisms are similar: higher Mohr-Coulomb slope allows the ice to resist breakup longer and creates larger floes (mimicking earlier, thicker ice situation); low air coefficient decreases ice drift and, consequently, ice deformation which again corresponds to an earlier period of RGPS observations.

375 After the first experiments, we observed the interannual trends in the  $P_0$  and  $c_{\text{ref}}$  parameters (see Figure 12). This leads us to conclude that the weak dependence of these rheology parameters on ice thickness (and potentially concentration) indicates that the parameterisation of  $P_{\text{max}}$  (see Eq. 2) requires optimised tuning of  $H$  and  $C$  parameters. That was the motivation to run the second experiment and to retrieve values of  $H$ ,  $C$  and  $C_A$ . Unfortunately, as table 4 shows, the accuracy of ML models for these parameters is not sufficiently high, and we cannot derive their optimal values. Nevertheless, accounting for these parameters in the second experiment allowed us to train ML models that show fewer diurnal variations and are more stable on interannual time scales. Moreover, despite low accuracy, the ML models predict lower values of  $H$  (1.38) and  $C$  (-28.7) than 380 the default ones. Dedicated experiments are needed to tune these parameters further.

## 6 Conclusions

We developed a new set of metrics for characterising the patterns in the sea ice deformation fields. These metrics are sensitive to the parameters of a sea ice model rheology and can be used to compare simulated and observed ice deformation for model evaluation or parameter tuning.

385 We developed a new method for tuning model parameters using machine learning. In our process, we train an ML model using simulated data and apply it to observations. In our case, the inputs to the ML model are the descriptors of sea ice deformation, and the targets are the sea ice rheology parameters. We tested a linear regression (LR) and a deep neural network

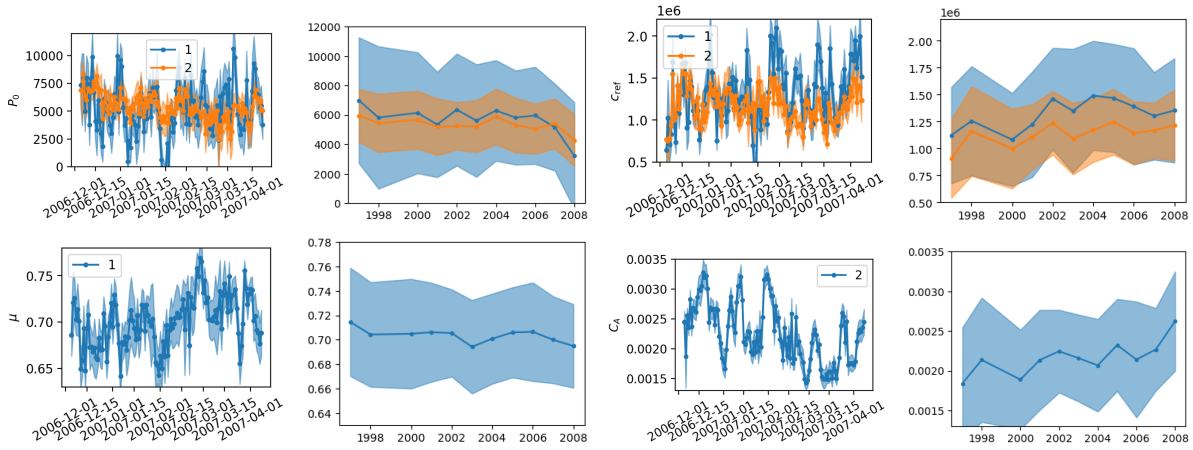


**Figure 12.** Time series of parameter values derived from RGPS for one year (left column) and several years (right column). Colour denotes the experiment, and the shaded area shows the standard deviation of samples produced by ten neural networks for the daily values (left column) or the samples collected from the entire year (right column).

(DNN) as ML models, and DNN always showed higher accuracy. This method can be applied to tune the parameters of any other model.

390 Using the new set of metrics and the new ML-based method, we found values of four BBM rheology parameters that were poorly constrained previously: scaling parameter for compressive strength ( $P_0 \approx 5.1$  kPa), cohesion at the reference scale ( $c_{\text{ref}} \approx 1.2$  MPa), internal friction angle tangent ( $\mu \approx 0.7$ ), ice–atmosphere drag coefficient ( $C_A \approx 0.00228$ ).

Our experiments cover a wide range of weather and sea ice conditions: from thin young ice in the Eastern Arctic to thick MYI near the Canadian Archipelago, from the beginning to the end of the freezing period, from calm days to winter storms. 395 Presumably, the ML model trained on such heterogeneous data is general enough to be applied in regions with similar ice conditions, e.g., Laptev, Kara, Barents, and Lincoln Seas in the Arctic or Weddel and Ross Seas in the Antarctic. Applying neXTSIM in the Antarctic shows that the model reproduces the seasonal cycle of sea ice extent and that BBM rheology simulates the sea ice drift with higher accuracy (Santana et al., 2024). In other regions (e.g., the Marginal Ice Zone), where the conditions are quite different, the sea ice concentration is lower, the ice elasticity drops substantially (see Eq. 4), the rheology 400 is no longer sensitive to  $c_{\text{ref}}$ ,  $P$ , or other parameters.

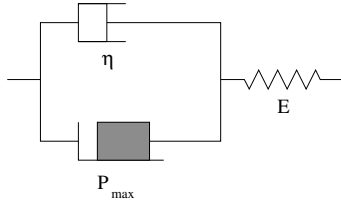
The tuned parameters exhibit weak interannual drift related to changes in sea ice thickness and corresponding changes in ice deformation patterns. Improving the dependence on thickness and concentration in the BBM rheology or tuning the corresponding parameters may reduce the drift and make the rheology completely independent of ice thickness influence. Recent observations of ice drift and deformation obtained from Sentinel-1 SAR data processing are recommended for tuning 405 the rheology to reflect the current situation and provide higher accuracy forecasts.

Other parameters in our experiments (exponent of compression factor, Poisson’s ratio, compaction parameter) did not impact the pattern of sea ice deformation, or the influence of other parameters masked their impact. Therefore, their values could not

be derived using our method. Dedicated experiments are required to study the sensitivity of the proposed metrics to these parameters and to tune their values.

410 **Appendix A: Additional figures**

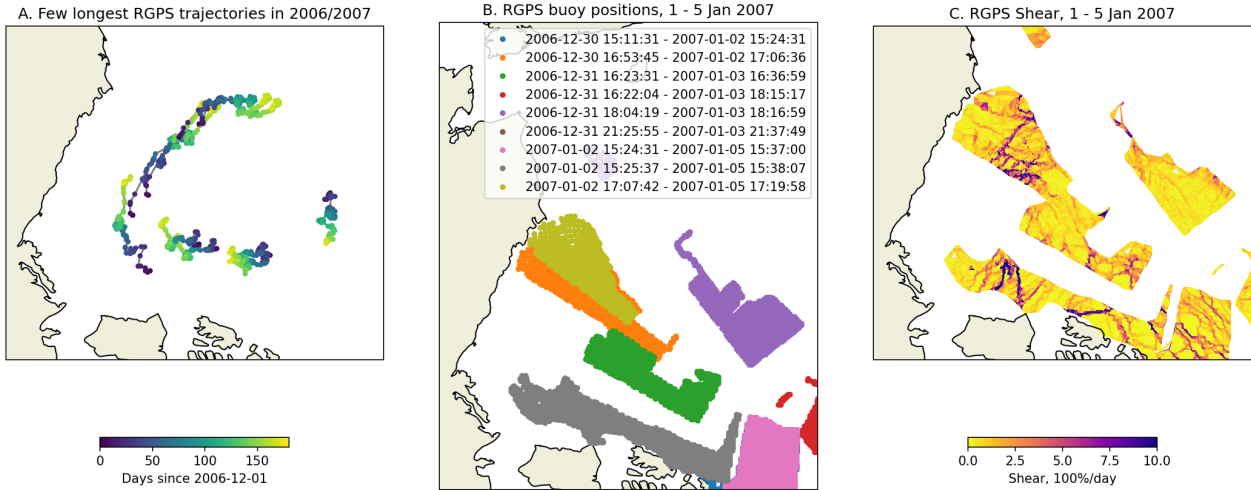
Figure A1 presents a scheme of the Bingham-Maxwell rheology, where a spring is connected in series with a block, where a dashpot and a friction element are connected in parallel.



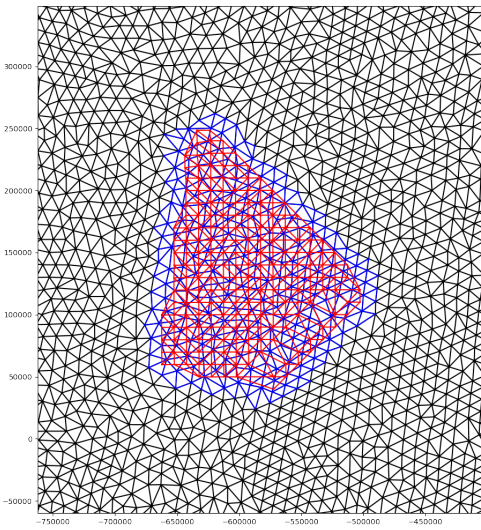
**Figure A1.** A schematic of the Bingham-Maxwell constitutive model showing a dashpot and a friction element connected in parallel, with both connected to a spring in series. The figure is adapted from (Ólason et al., 2022).

Figure A2.A shows examples of RGPS trajectories spanning 150 – 180 days, and A2.B shows positions of virtual buoys detected on SAR images acquired between 1<sup>st</sup> and 5<sup>th</sup> Jan 2007. Points are coloured by the time of image acquisition. Panel  
415 C on Figure A2 shows the shear component of deformation computed from the drift of buoys shown on panel B. The figure illustrates how heterogeneous the RGPS Lagrangian ice motion data is in space and time.

Figure A3 shows a collocation of a neXtSIM mesh (shown in black colour) and a triangulated subset from the RGPS dataset (shown in red colour). The RGPS subset is created by selecting starting and ending virtual buoy positions belonging to the same Radarsat-1 images separated by 3 days. All nodes on the neXtSIM mesh within 10 km from the RGPS subset are selected  
420 (blue colour) and used for the computation of deformation.



**Figure A2.** **A.** Example trajectories of virtual buoys detected on Radarsat-1 data by the RGPS system between 1<sup>st</sup> December 2006 and 15<sup>th</sup> May 2007. **B.** Position of virtual buoys on SAR images acquired between 1<sup>st</sup> and 5<sup>th</sup> January 2007. Points are coloured by the starting and ending image acquisition time, as shown in the legend. **C.** Shear computed from the Radarsat-1 image pairs shown on **B**.



**Figure A3.** Illustration of RGPS and neXtSIM mesh collocation. The neXtSIM mesh from one snapshot is shown in black. The RGPS mesh created by triangulation of virtual drifters detected on a pair of Radarsat-2 images is shown in red. The neXtSIM mesh subsampled from the original mesh for collocation with the RGPS mesh is shown in blue.

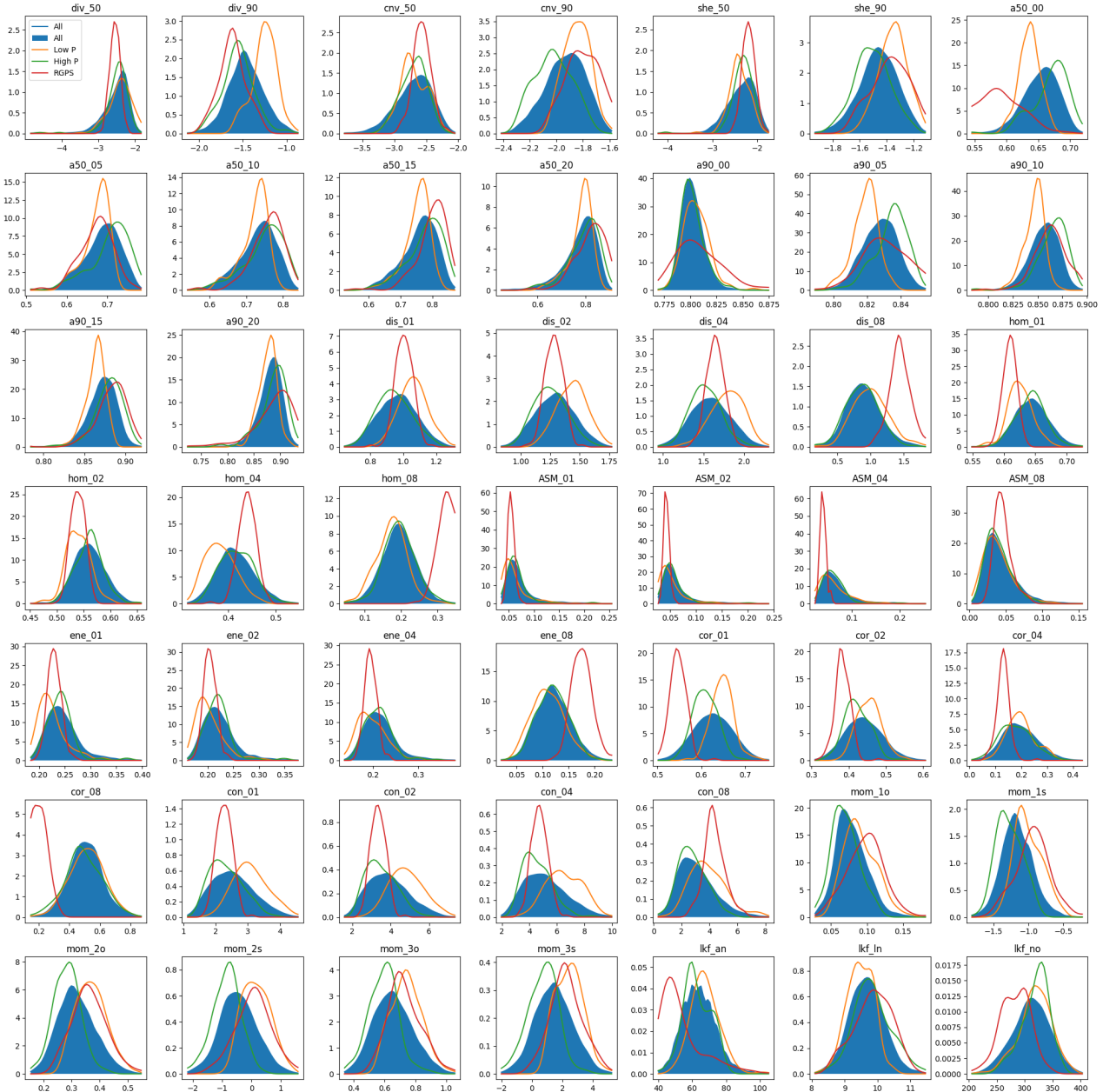


**Figure A4.** PDFs of all deformation descriptors for RGPS (red), all neXtSIM runs (blue), and runs with lowest (orange) or highest values of  $P_0$ .

*Code and data availability.* The code for processing RGPS and neXtSIM data and computing ice deformation descriptors is publicly available on GitHub (Korosov, 2024c).

The code for tuning the neXtSIM BBM parameters and preparing the figures for the manuscript is publicly available on GitHub (Korosov, 2024b).

425 Samples of neXtSIM data used in the study are publicly available on Zenodo (Korosov, 2024a).

RGPS data is publicly available on the Alaska Satellite Facility: <https://ASF.alaska.edu/datasets/daac/sea-ice-measures/>.

*Author contributions.* AK, YY and EO designed the experiment and wrote the manuscript. EO developed the BBM rheology and largely contributed to the development of the netXSIM. AK developed the code for computing the metrics and running the ML-based parameter tuning. AK ran all the experiments.

430 *Competing interests.* The authors declare that no competing interests are present.

*Acknowledgements.* We acknowledge the support from the Research Council of Norway (project "Multi-scale Sea Ice Code", no. 325292) and the support from the Norwegian Space Agency (project "Synergy of SAR, radiometry, and altimetry for Digital Arctic Sea Ice Twin", no. 74CO2221). We are thankful to Pierre Rampal for fruitful discussions of methodology for image anisotropy computation and the results of the experiments.

Bouillon, S. and Rampal, P.: Presentation of the dynamical core of neXtSIM, a new sea ice model, *Ocean Modelling*, 91, 23–37, <https://doi.org/10.1016/j.ocemod.2015.04.005>, 2015.

Boutin, G., Williams, T., Horvat, C., and Brodeau, L.: Modelling the Arctic wave-affected marginal ice zone: a comparison with ICESat-2 observations, *Philosophical Transactions of the Royal Society A: Mathematical, Physical and Engineering Sciences*, 380, 440 <https://doi.org/10.1098/rsta.2021.0262>, 2022.

Boutin, G., Ólason, E., Rampal, P., Regan, H., Lique, C., Talandier, C., Brodeau, L., and Ricker, R.: Arctic sea ice mass balance in a new coupled ice–ocean model using a brittle rheology framework, *The Cryosphere*, 17, 617–638, <https://doi.org/10.5194/tc-17-617-2023>, 2023.

445 Brodeau, L., Rampal, P., Ólason, E., and Dansereau, V.: Implementation of a brittle sea-ice rheology in an Eulerian, finite-difference, C-grid modeling framework: Impact on the simulated deformation of sea-ice in the Arctic, *Geoscientific Model Development Discussions*, 2024, 1–46, <https://doi.org/10.5194/gmd-2023-231>, 2024.

Chen, Y., Smith, P., Carrassi, A., Pasman, I., Bertino, L., Bocquet, M., Finn, T. S., Rampal, P., and Dansereau, V.: Multivariate state and parameter estimation with data assimilation applied to sea-ice models using a Maxwell elasto-brittle rheology, *The Cryosphere*, 18, 2381–2406, <https://doi.org/10.5194/tc-18-2381-2024>, 2024.

450 Dansereau, V., Weiss, J., Saramito, P., and Lattes, P.: A Maxwell elasto-brittle rheology for sea ice modelling, *Cryosphere*, 10, 1339–1359, <https://doi.org/10.5194/tc-10-1339-2016>, 2016.

Dierking, W., Stern, H. L., and Hutchings, J. K.: Estimating statistical errors in retrievals of ice velocity and deformation parameters from satellite images and buoy arrays, *The Cryosphere*, 14, 2999–3016, <https://doi.org/10.5194/tc-14-2999-2020>, 2020.

455 Girard, L., Bouillon, S., Weiss, J., Amitrano, D., Fichefet, T., and Legat, V.: A new modeling framework for sea-ice mechanics based on elasto-brittle rheology, *Annals of Glaciology*, 52, 123–132, <https://doi.org/10.3189/172756411795931499>, 2011.

Haralick, R. M., Shanmugam, K., and Dinstein, I.: Textural Features for Image Classification, *IEEE Transactions on Systems, Man, and Cybernetics, SMC-3*, 610–621, <https://doi.org/10.1109/TSMC.1973.4309314>, 1973.

Hersbach, H., Bell, B., Berrisford, P., Hirahara, S., Horányi, A., Muñoz-Sabater, J., Nicolas, J., Peubey, C., Radu, R., Schepers, D., Simmonds, A., Soci, C., Abdalla, S., Abellán, X., Balsamo, G., Bechtold, P., Biavati, G., Bidlot, J., Bonavita, M., De Chiara, G., Dahlgren, 460 P., Dee, D., Diamantakis, M., Dragani, R., Flemming, J., Forbes, R., Fuentes, M., Geer, A., Haimberger, L., Healy, S., Hogan, R. J., Hólm, E., Janisková, M., Keeley, S., Laloyaux, P., Lopez, P., Lupu, C., Radnoti, G., de Rosnay, P., Rozum, I., Vamborg, F., Vil- laume, S., and Thépaut, J.-N.: The ERA5 global reanalysis, *Quarterly Journal of the Royal Meteorological Society*, 146, 1999–2049, <https://doi.org/10.1002/qj.3803>, 2020.

Hibler, W. D.: A dynamic thermodynamic sea ice model, *Journal of Physical Oceanography*, 9, 815–846, [https://doi.org/10.1175/1520-0485\(1979\)009<0815:adtsim>2.0.co;2](https://doi.org/10.1175/1520-0485(1979)009<0815:adtsim>2.0.co;2), 1979.

Hinton, G. E. and Salakhutdinov, R. R.: Reducing the Dimensionality of Data with Neural Networks, *Science*, 313, 504–507, <https://doi.org/10.1126/science.1127647>, 2006.

Hopkins, M. A.: Four stages of pressure ridging, *Journal of Geophysical Research: Oceans*, 103, 21 883–21 891, <https://doi.org/10.1029/98JC01257>, 1998.

470 Hutter, N. and Losch, M.: Feature-based comparison of sea ice deformation in lead-permitting sea ice simulations, *The Cryosphere*, 14, 93–113, <https://doi.org/10.5194/tc-14-93-2020>, 2020.

Hutter, N., Zampieri, L., and Losch, M.: Leads and ridges in Arctic sea ice from RGPS data and a new tracking algorithm, *The Cryosphere*, 13, 627–645, <https://doi.org/10.5194/tc-13-627-2019>, 2019.

Kingma, D. P. and Ba, J.: Adam: A Method for Stochastic Optimization, <https://arxiv.org/abs/1412.6980>, 2017.

475 Korosov, A.: Outputs of the next generation sea ice model (neXtSIM) for winter 2006 - 2007 saved for comparison with RGPS., <https://doi.org/10.5281/zenodo.13302007>, 2024a.

Korosov, A.: NeXtSIM parameter tuning software, nextsimtuning-0.1, <https://doi.org/10.5281/zenodo.13302227>, 2024b.

Korosov, A.: Sea ice drift deformation analysis software, pysida-0.1, <https://doi.org/10.5281/zenodo.13301869>, 2024c.

480 Korosov, A., Rampal, P., Ying, Y., Ólason, E., and Williams, T.: Towards improving short-term sea ice predictability using deformation observations, *The Cryosphere*, 17, 4223–4240, <https://doi.org/10.5194/tc-17-4223-2023>, 2023.

Kwok, R.: Contrasts in sea ice deformation and production in the Arctic seasonal and perennial ice zones, *Journal of Geophysical Research*, 111, <https://doi.org/10.1029/2005jc003246>, 2006.

Kwok, R., Hunke, E. C., Maslowski, W., Menemenlis, D., and Zhang, J.: Variability of sea ice simulations assessed with RGPS kinematics, *Journal of Geophysical Research*, 113, <https://doi.org/10.1029/2008JC004783>, 2008.

485 Lehoucq, R., Weiss, J., Dubrulle, B., Amon, A., Le Bouil, A., Crassous, J., Amitrano, D., and Graner, F.: Analysis of image vs. position, scale and direction reveals pattern texture anisotropy, *Frontiers in Physics*, 2, <https://doi.org/10.3389/fphy.2014.00084>, 2015.

Marsan, D. and Weiss, J.: Space/time coupling in brittle deformation at geophysical scales, *Earth and Planetary Science Letters*, 296, 353–359, <https://doi.org/10.1016/j.epsl.2010.05.019>, 2010.

490 Massonnet, F., Goosse, H., Fichefet, T., and Counillon, F.: Calibration of sea ice dynamic parameters in an ocean-sea ice model using an ensemble Kalman filter, *Journal of Geophysical Research: Oceans*, 119, 4168–4184, <https://doi.org/10.1002/2013jc009705>, 2014.

McKay, M. D., Beckman, R. J., and Conover, W. J.: A Comparison of Three Methods for Selecting Values of Input Variables in the Analysis of Output from a Computer Code, *Technometrics*, 21, 239–245, <http://www.jstor.org/stable/1268522>, 1979.

Mellor, M.: Mechanical behavior of sea ice, chap. 2, pp. 165–281, NATO ASI Series, Springer US, Boston, MA, [https://doi.org/10.1007/978-1-4899-5352-0\\_3](https://doi.org/10.1007/978-1-4899-5352-0_3), 1986.

495 Ólason, E., Boutin, G., Korosov, A., Rampal, P., Williams, T., Kimmritz, M., Dansereau, V., and Samaké, A.: A new brittle rheology and numerical framework for large-scale sea-ice models, *Journal of Advances in Modeling Earth Systems*, 14, <https://doi.org/10.1029/2021ms002685>, 2022.

Panteleev, G., Yaremchuk, M., Stroh, J. N., Francis, O. P., and Allard, R.: Parameter optimization in sea ice models with elastic–viscoplastic rheology, *The Cryosphere*, 14, 4427–4451, <https://doi.org/10.5194/tc-14-4427-2020>, 2020.

500 Panteleev, G., Yaremchuk, M., and Francis, O.: Reconstruction of the Rheological Parameters in a Sea Ice Model with Viscoplastic Rheology, *Journal of Atmospheric and Oceanic Technology*, 40, 141 – 157, <https://doi.org/10.1175/JTECH-D-21-0158.1>, 2023.

Park, J.-W., Korosov, A. A., Babiker, M., Won, J.-S., Hansen, M. W., and Kim, H.-C.: Classification of Sea Ice Types in Sentinel-1 SAR images, *The Cryosphere Discussions*, 2019, 1–23, <https://doi.org/10.5194/tc-2019-127>, 2019.

Rampal, P., Bouillon, S., Ólason, E., and Morlighem, M.: neXtSIM: a new Lagrangian sea ice model, *The Cryosphere*, 10, 1055–1073, <https://doi.org/10.5194/tc-10-1055-2016>, 2016.

505 Rampal, P., Dansereau, V., Ólason, E., Bouillon, S., Williams, T., Korosov, A., and Samaké, A.: On the multi-fractal scaling properties of sea ice deformation, *The Cryosphere*, 13, 2457–2474, <https://doi.org/10.5194/tc-13-2457-2019>, 2019.

Regan, H., Rampal, P., Ólason, E., Boutin, G., and Korosov, A.: Modelling the evolution of Arctic multiyear sea ice over 2000–2018, *The Cryosphere*, 17, 1873–1893, <https://doi.org/10.5194/tc-17-1873-2023>, 2023.

510 Sakov, P., Counillon, F., Bertino, L., Lister, K. A., Oke, P. R., and Koralev, A.: TOPAZ4: An ocean sea ice data assimilation system for the  
North Atlantic and Arctic, *Ocean Science*, 8, 633–656, <https://doi.org/10.5194/os-8-633-2012>, 2012.

Santana, R., Boutin, G., Horvat, C., Ólason, E., Williams, T., and Rampal, P.: Modelling Antarctic sea ice variability using a brittle rheology,  
<https://doi.org/10.5281/zenodo.10637222>, 2024.

Schluson, E. M., Fortt, A. L., Iliescu, D., and Renshaw, C. E.: Failure envelope of first-year Arctic sea ice: The role of friction in compressive  
515 fracture, *Journal of Geophysical Research*, 111, <https://doi.org/10.1029/2005JC003235>, 2006.

Tsamados, M., Feltham, D. L., and Wilchinsky, A. V.: Impact of a new anisotropic rheology on simulations of Arctic sea ice, *Journal of  
Geophysical Research: Oceans*, 118, 91–107, <https://doi.org/10.1029/2012jc007990>, 2013.

van der Walt, S., Schönberger, J., Nunez-Iglesias, J., Boulogne, F., Warner, J., Yager, N., Gouillart, E., and Yu, T.: scikit-image: image  
processing in Python, *PeerJ*, <https://doi.org/10.7717/peerj.453>, 2014.

520 Vincent, P., Larochelle, H., Bengio, Y., and Manzagol, P.-A.: Extracting and composing robust features with denoising autoencoders, in:  
International Conference on Machine Learning, <https://api.semanticscholar.org/CorpusID:207168299>, 2008.

Weiss, J. and Schulson, E. M.: Coulombic faulting from the grain scale to the geophysical scale: lessons from ice, *Journal of Physics D:  
Applied Physics*, 42, 214017, <https://doi.org/10.1088/0022-3727/42/21/214017>, 2009.

Wilchinsky, A. V. and Feltham, D. L.: A continuum anisotropic model of sea-ice dynamics, *Proceedings of the Royal Society of London.  
525 Series A: Mathematical, Physical and Engineering Sciences*, 460, 2105–2140, <https://doi.org/10.1098/rspa.2004.1282>, 2004.

Williams, T., Korosov, A., Rampal, P., and Ólason, E.: Presentation and evaluation of the Arctic sea ice forecasting system neXtSIM-F, *The  
Cryosphere*, 15, 3207–3227, <https://doi.org/10.5194/tc-15-3207-2021>, 2021.

Zakhvatkina, N., Korosov, A., Muckenhuber, S., Sandven, S., and Babiker, M.: Operational algorithm for ice–water classification on  
dual-polarized RADARSAT-2 images, *The Cryosphere*, 11, 33–46, <https://doi.org/10.5194/tc-11-33-2017>, 2017.

530 Zhang, Y.-F., Bitz, C. M., Anderson, J. L., Collins, N. S., Hoar, T. J., Raeder, K. D., and Blanchard-Wrigglesworth, E.: Estimating parameters  
in a sea ice model using an ensemble Kalman filter, *The Cryosphere*, 15, 1277–1284, <https://doi.org/10.5194/tc-15-1277-2021>, 2021.

Zwally, H. J., Schutz, R. H., and Dimarzio, J.: GLAS/ICESat L2 Sea Ice Altimetry Data.,  
<https://doi.org/10.5067/ICESAT/GLAS/DATA210>, 2014.